

Incremental Rotation Averaging Revisited and More: A New Rotation Averaging Benchmark

Xiang Gao, Hainan Cui, and Shuhan Shen, *Senior Member, IEEE*

Abstract—In order to further advance the accuracy and robustness of the incremental parameter estimation-based rotation averaging methods, in this paper, a new member of the Incremental Rotation Averaging (IRA) family is introduced, which is termed as IRAv4. As the most significant feature of the IRAv4, a task-specific connected dominating set is extracted to serve as a more reliable and accurate reference for rotation global alignment. In addition, to further address the limitations of the existing rotation averaging benchmark of relying on the slightly outdated Bundler camera calibration results as ground truths and focusing solely on rotation estimation accuracy, this paper presents a new COLMAP-based rotation averaging benchmark that incorporates a cross check between COLMAP and Bundler, and employ the accuracy of both rotation and downstream location estimation as evaluation metrics, which is desired to provide a more reliable and comprehensive evaluation tool for the rotation averaging research. Comprehensive comparisons between the proposed IRAv4 and other mainstream rotation averaging methods on this new benchmark demonstrate the effectiveness of our proposed approach.

Index Terms—Large-scale rotation averaging, task-specific connected dominating set, rotation averaging benchmarking.

I. INTRODUCTION

MAGE-based large-scale scene 3D reconstruction is a fundamental task in computer vision community, which has been widely investigated in recent years [1], [2], [3], [4]. As its core step, Structure from Motion (SfM) [5], [6], [7], [8], [9] aims to simultaneously recover camera pose and scene structure given pair-wise image feature matches. According to the camera pose initialization scheme, SfM methods could be roughly divided into incremental and global ones. The camera poses are sequentially estimated in incremental SfM via a iterative optimization pipeline [6], [8], but are simultaneously solved in global SfM by the motion averaging methodology [5], [9]. Compared with incremental SfM methods, global ones feature fewer optimization iterations and estimation parameters, which makes them with more advantage in theory and greater potential for application when dealing with increasingly larger reconstruction scene scales.

Motion averaging, which takes relative camera motions (rotations and translations) as input and produces absolute camera poses (orientations and locations), is the primary technique used for camera pose recovery in global SfM. Due to scale ambiguity of the relative translation estimated via essential

X. Gao, H. Cui, and S. Shen are with the Institute of Automation, Chinese Academy of Sciences (CASIA), Beijing 100190, China, the School of Artificial Intelligence, University of Chinese Academy of Sciences, Beijing 100049, China, and also with the CASIA-SenseTime Research Group, Beijing 100190, China (e-mail: xiang.gao@ia.ac.cn; hainan.cui@ia.ac.cn; shshen@nlpr.ia.ac.cn).

matrix decomposition [10], motion averaging is conducted in the manner of first rotation and then translation averaging in most cases. As the former of the above two phases, rotation averaging [11] directly influences the effect of the subsequent translation averaging phase, and even all the remaining 3D reconstruction procedure, *e.g.* multi-view triangulation for scene recovery and global Bundle Adjustment (BA) for parameter optimization. Though increasing attention has been drawn in recent years [12], [13], [14], [15], [16], [17], [18], [19], [20], the problem of rotation averaging is still far from being solved due to the large scale, imbalanced connectivity, and high-level noise in the Epipolar-geometry Graph (EG).

Recently, a series of rotation averaging methods [21], [22], [23], [24] are proposed based on the ideology of incremental parameter estimation stemmed from incremental SfM. As the primitive and primary method, Incremental Rotation Averaging (IRA) [21] performs incremental absolute rotation computation and relative rotation outlier filtering simultaneously, by which the rotation estimation accuracy and robustness are both guaranteed. To further enhance the efficiency and scalability, IRA++ [22] is proposed, where the input EG is clustered to construct several low-level intra-sub-EGs and a high-level inter-one. Then IRA is performed on all the (intra- and inter-) sub-EGs to achieve local estimation and global alignment of absolute rotations, respectively. In order to achieve a task-specific EG clustering for better rotation averaging performance, IRAv3 [23] is presented, where the cluster affiliation of each camera is dynamically determined with its absolute rotation (in the local coordinate system of intra-sub-EG) simultaneously estimated. To accomplish a better global alignment of the local rotation estimates, inspired by Jiang *et al.* [25], IRAv3+ [24] is introduced. Instead of performing a cluster-level rotation averaging, which is done in both IRA++ and IRAv3, multiple Connected Dominating Sets (CDSs) are randomly extracted to serve as the reference for rotation local-to-global alignment.

However, in this paper we argue that the accuracy and robustness of the IRA series described above could be advanced one step further. Though the effectiveness of the cluster-based pipeline with task-independent CDS serving as global reference has been demonstrated in both IRAv3+ [24] and Jiang *et al.* [25], we believe that with a task-specific CDS extracted, more reliable global reference construction together with more accurate camera pose globalization would be further achieved. Based on the above analysis, a novel rotation averaging method termed as IRAv4 is proposed in this paper, which is built upon IRAv3+. The major difference between them lies in that instead of first extracting multiple CDSs and then

estimating the absolute rotations in the CDSs' local coordinate system by leveraging IRA, which is done in IRAv3+, the (task-specific) CDS is extracted by incrementally selecting the Next-Best Vertex (NBV) to maximize the supports from the currently extracted ones in the CDS, together with its absolute rotation (in the local coordinate system of CDS) simultaneously estimated.

Moreover, we find two issues that need to be addressed when evaluating the performance of most existing rotation averaging methods [26], [27], [28], [29], [16], [21], [30], [19], [31], [22], [23], [24]. Firstly, the evaluation is mostly performed based on the 1DSfM [32] dataset with the camera calibration results of the slightly outdated Bundler [33] serving as ground truth. And secondly, the evaluation mostly focuses on the camera rotation estimation accuracy only while ignoring the influence of the estimated rotations to the downstream task, *i.e.* translation averaging. To deal with these, a new COLMAP-based [6] rotation averaging benchmark is rebuilt upon the 1DSfM dataset in this paper, where the EG of each test data in the 1DSfM dataset¹ is regenerated by leveraging COLMAP² and OpenCV³ libraries. To provide a more reliable ground-truth source, only the camera poses pass the cross check between COLMAP and Bundler are employed in this new benchmark. In order to additionally evaluate the effectiveness of the estimated rotations for the downstream translation averaging task, in our new benchmark, the rotations estimated by different rotation averaging methods, together with the relative translations in the regenerated EG, are feed into a well-established translation averaging method, BATA [34], to obtain absolute camera locations for location estimation accuracy evaluation. Based on the new benchmark, comprehensive evaluation is performed on the proposed IRAv4 and several currently mainstream rotation averaging methods, including the existing IRA series [21], [22], [23], [24], and some other methods [35], [26], [27], [30], [31], [28]. Among all these methods for performance evaluation, the proposed IRAv4 in this paper achieves state of the art in both rotation estimation and the downstream location estimation on the new benchmark, by which its effectiveness is demonstrated.

The main contributions of this paper are threefold:

- 1) A novel cluster-based rotation averaging pipeline is proposed, where a task-specific CDS is extracted to serve as the global reference for rotation local-to-global alignment.
- 2) A new rotation averaging benchmark based on the 1DSfM dataset and the COLMAP library is presented, where both the ground truth source and the performance evaluation metrics are redefined for a more reliable and comprehensive evaluation.
- 3) A comprehensive evaluation is conducted between the proposed IRAv4 and several mainstream rotation averaging methods on the new benchmark, where state-of-the-art performance of IRAv4 is achieved to demonstrate its effectiveness.

II. BRIEF DESCRIPTION ON THE IRA SERIES

Before introducing the proposed IRAv4 method in this paper, brief descriptions on the existing IRA series, including

IRA [21], IRA++ [22], IRAv3 [23], and IRAv3+ [24], are provided for their better understanding. And more details on them could be found in the original papers.

IRA [21] mainly has two steps: 1) The camera triplet with minimum cyclic rotation deviation after local optimization is selected as the initial seed and its optimized absolute rotations (in the camera triplet's local coordinate system) are served as the seed estimation. 2) The camera with most supporting EG edges during chaining-based absolute rotation pre-computation is selected as the NBV and the pre-computed absolute rotation is served as its initialization; and then, either local (on the newest estimated absolute rotation only) or global optimization (on all the currently estimated absolute rotations) is performed. Note that inlier/outlier relative rotation measurements related to the absolute rotations to be optimized could be distinguished based on their current estimates, and only the inliers are involved in the above optimization. The NBV selection, initialization, and optimization are iteratively performed until all the absolute rotations have been estimated.

IRA++ [22] contains five steps: 1) Community detection-based EG clustering [36] is carried out on the input EG to obtain several intra-sub-EGs. 2) IRA is performed on each low-level intra-sub-EG to estimate the cameras' absolute rotations in its local coordinate system. 3) Voting-based single rotation averaging [29] is conducted to estimate the relative rotation between the local coordinate systems of each intra-sub-EG pair. 4) IRA is performed again on the high-level inter-sub-EG to estimate the absolute rotation of each intra-sub-EG's local coordinate system. 5) And finally, rotation global alignment and optimization is conducted to first globally align the absolute rotations of all the vertices in the input EG to a uniform coordinate system, and then globally optimize them to produce the final rotation averaging result.

IRAv3 [23] comprises five steps as well, with its last three steps similar to those of IRA++. And for the first two: 1) Community detection-based seed construction is performed to construct several cluster seeds for the follow-up on-the-fly procedures in its second step. 2) On-the-fly EG clustering and intra-sub-EG rotation estimation are conducted to dynamically assign unregistered vertices to certain EG clusters and iteratively estimate their absolute rotations in their assigned clusters' local coordinate systems. The second step is the core one of IRAv3 and contains three sub-steps, including potential cluster and vertex pre-selection, NBV selection and cluster affiliation, and incremental absolute rotation computation, with the last two iteratively performed for the on-the-fly procedures.

IRAv3+ [24] consists of five steps once again, which shares the same first two and last one steps with IRAv3 for 1) and 2) on-the-fly EG clustering and intra-sub-EG rotation estimation, and 5) rotation global alignment and optimization, respectively. After executing the first two steps for dynamic vertex cluster affiliation and rotation estimation, the third and forth ones are sequentially conducted: 3) Multiple CDSs are randomly extracted and IRA is performed on the CDSs-based sub-EG for global alignment reference construction. 4) Cluster-wise relative rotation for rotation local-to-global alignment is estimated by leveraging the guidance of the cluster-to-reference common vertices. Subsequently, similar to both IRA++ and IRAv3, the

¹<https://www.cs.cornell.edu/projects/1dsfm/>

²<https://demuc.de/colmap/>

³<https://opencv.org/>

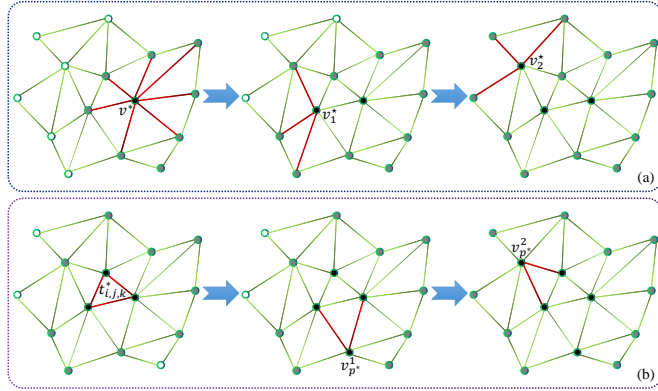


Fig. 1. Toy examples of the traditional method (a) based on an approximation algorithm [37] and the task-specific method (b) proposed in IRAv4 for Connected Dominating Set (CDS) extraction. For (a), the red edges denote those between the currently selected vertex (v^* or v_i^* , where v_i^* denotes the selected vertex in the i -th iteration) and its adjacent unselected ones. And for (b), the red edges denote those of the selected triplet $t_{i,j,k}^*$ and the edge supporting set for the selected Next-Best Vertex (NBV) v_p^i in the initialization step and the i -th iteration step, respectively. It could be observed from the figure that the number of vertices in the task-specific CDS is usually larger than that of the CDS extracted in the traditional way (5 vs. 3 in this toy example). Please refer to the main text for more details.

local absolute rotations in each cluster are firstly globally aligned to a uniform coordinate system (that of the CDSs-based sub-EG for IRAv3+), and then globally optimized.

III. THE PROPOSED IRAv4 METHOD

The proposed IRAv4 in this paper is directly built upon the IRAv3+ [24], and the major difference between them is the manner of global reference construction. It should be noted that the process of global reference construction involves two sub-steps of 1) reference-based sub-EG extraction and 2) sub-EG rotation estimation. Based on the description in the last section, the above two sub-steps in IRAv3+ are conducted sequentially to result in a task-independent global reference. However, for our proposed IRAv4, it follows the incremental parameter estimation pipeline during the global reference construction, where the vertices in the reference-based sub-EG are incrementally selected together with their absolute rotations simultaneously estimated. By this way, a task-specific reference for rotation local-to-global alignment is constructed. The process of the task-specific reference construction is detailed in the following. Before that, the rotation averaging problem is briefly formulated for better understanding at first: The input EG is denoted as $\mathcal{G} = (\mathcal{V}, \mathcal{E})$, where \mathcal{V} and \mathcal{E} denote the sets of cameras and camera pairs with sufficient image local feature match inliers for essential matrix estimation, and the rotation averaging problem is defined as given the relative rotation measurements $\{\mathbf{R}_{i,j} | e_{i,j} \in \mathcal{E}\}$, and estimating the absolute camera orientations $\{\mathbf{R}_i | v_i \in \mathcal{V}\}$.

A. Task-Specific CDS-Based Global Reference Construction

Similar to Jiang *et al.* [25] and IRAv3+ [24], CDS-based sub-EG is also used to serve as a global reference for camera pose alignment in IRAv4. The CDS problem in graph theory asks for a *minimum-size* and *connected* subset of vertices

with the following property which accounts for the concept of *dominating*: Each vertex is required to either be in the CDS, or adjacent to some vertex of the CDS. The CDS problem is usually solved based on an approximation algorithm [37], which roughly proceeds as follows:

Init: Mark all vertices in \mathcal{V} white. Select the vertex v^* with most neighbours in a weighted or unweighted manner. Mark v^* and its neighbours black and gray, respectively.

Iter: For all the gray vertices, select the vertex v^* with most white neighbours in a weighted or unweighted manner. Mark v^* and its white neighbours in black and gray, respectively. Iterate the above step until there is no white vertex in \mathcal{V} , and the black vertex set constitutes the CDS.

Fig. 1(a) gives a toy example on the traditional (or task-independent) CDS extraction procedure described above.

However, in this paper we claim that compared with the task-independent CDS extracted based on graph theory, a task-specific CDS would provide a more reliable global reference for camera rotation alignment, by which more accurate and robust rotation estimation could be achieved. The procedure of the task-specific CDS extraction in this paper is stemmed from the pipeline of IRA [21], and the major difference between them are the termination conditions. As described in the last section, IRA's iteration of NBV selection, initialization, and optimization stops until all the absolute rotations of the vertices in \mathcal{V} have been estimated and optimized. Nevertheless, the task-specific CDS extraction in IRAv4 shares the termination condition of the traditional CDS extraction to guarantee that it is extracted to exhibit the properties of *connected* and *dominating*, *i.e.* the vertices in the CDS are connected and all the vertices in \mathcal{V} is either in or adjacent to some vertex of the CDS. Note that during the extraction of the task-specific CDS in IRAv4, the absolute rotations of the extracted vertices are simultaneously estimated, and the property of *minimum* in size is no longer guaranteed. In fact, as the vertex with higher reliability instead of larger coverage is selected with priority, the number of vertices in the task-specific CDS of IRAv4 is always larger than that of the task-independent one extracted by the traditional method [37]. The task-specific CDS extraction procedure for global reference construction, which is illustrated by a toy example in Fig. 1(b)), is detailed in the following.

For the *initialization* step, the camera triplet set in \mathcal{G} is obtained and denoted as \mathcal{T} , and for each triplet $t_{i,j,k} \in \mathcal{T}$, similar to IRA, the absolute rotations of $\{v_i, v_j, v_k\}$ in the triplet's local coordinate system are initialized and optimized by measurement chaining and residual minimization of the relative rotations, by which the CDS's initial triplet is selected together with the absolute rotations estimated. Specifically, the absolute rotations in $t_{i,j,k}$ are firstly initialized as:

$$\mathbf{R}_i = \mathbf{I}, \mathbf{R}_j = \mathbf{R}_{i,j}, \mathbf{R}_k = \mathbf{R}_{i,k}, \quad (1)$$

and then fed into the following triplet-based chaining check:

$$d_{\mathbf{R}}(\mathbf{R}_{j,k}, \mathbf{R}_{i,k} \mathbf{R}_{i,j}^{\top}) < \theta_{\text{th}}, \quad (2)$$

where $d_{\mathbf{R}}(\mathbf{R}_1, \mathbf{R}_2) = \arccos \frac{\text{tr}(\mathbf{R}_2 \mathbf{R}_1^{\top}) - 1}{2}$ is the angular distance between two rotation matrices, \mathbf{R}_1 and \mathbf{R}_2 , and $\theta_{\text{th}} = 3^\circ$

is the outlier threshold in this paper. The triplet set that passes the above chaining check, \mathcal{T}' , is involved in the following optimization for initial seed selection and estimation:

$$\mathbf{R}_i^*, \mathbf{R}_j^*, \mathbf{R}_k^* = \arg \min \sum_{\substack{v_i, v_j \in \mathcal{V}_{t_{i,j,k}} \\ e_{i,j} \in \mathcal{E}_{t_{i,j,k}}}} d_{\mathbf{R}}^2(\mathbf{R}_{i,j}, \mathbf{R}_j \mathbf{R}_i^\top), \quad (3)$$

the above optimization problem and the other ones in the rest of this paper are solved by the Ceres Solver library⁴, and the triplet $t_{i,j,k}^* = \{v_{i^*}, v_{j^*}, v_{k^*}\}$ with the largest selection reward defined in the following, together with the optimized rotations $\{\mathbf{R}_i^*, \mathbf{R}_j^*, \mathbf{R}_k^*\}$ are served as the initial seed construction:

$$t_{i,j,k}^* = \arg \max_{t_{i,j,k} \in \mathcal{T}'} \sum_{\substack{v_i, v_j \in \mathcal{V}_{t_{i,j,k}} \\ e_{i,j} \in \mathcal{E}_{t_{i,j,k}}}} \cos(d_{\mathbf{R}}(\mathbf{R}_{i,j}, \mathbf{R}_j^* \mathbf{R}_i^{*\top})). \quad (4)$$

For the *iteration* step, the vertex sets of the currently selected and not selected to the global reference are denoted as \mathcal{V}^s and \mathcal{V}^t , respectively. Note that the absolute rotations of all the vertices in \mathcal{V}^s have been estimated in \mathcal{V}^s 's local coordinate system, which are denoted as $\{\mathbf{R}_m | v_m \in \mathcal{V}^s\}$. And the vertex v_{p^*} in \mathcal{V}^t that receives largest supports from \mathcal{V}^s is selected from \mathcal{V}^t to \mathcal{V}^s together with its rotation firstly initialized and then optimized. This iteration step of selection, initialization, and optimization stops until the (connecting and dominating) termination conditions of the task-specific CDS construction reaches, and then the current \mathcal{V}^s together with the estimated absolute rotations of the vertices in \mathcal{V}^s are served as the global reference constructed by IRAv4. Specifically, for each vertex v_p in \mathcal{V}^t , the edge set between it and \mathcal{V}^s is obtained and denoted as \mathcal{E}_p , and for each edge $e_{m,p}$ in \mathcal{E}_p connecting v_m in \mathcal{V}^s and v_p in \mathcal{V}^t , the pre-computing set of v_p 's absolute rotation is obtained by:

$$\{\mathbf{R}_p^m = \mathbf{R}_{m,p} \mathbf{R}_m | v_m \in \mathcal{V}^s, v_p \in \mathcal{V}^t, e_{m,p} \in \mathcal{E}_p\}. \quad (5)$$

Though the items in $\{\mathbf{R}_p^m\}$ represent the absolute rotation pre-computations of the same vertex v_p , the ideal identity is hard to hold practically due to the inevitable errors in both $\mathbf{R}_{m,p}$ and \mathbf{R}_m . To deal with this, similar to IRA, the supporting set of each item in the pre-computing set defined in Eq. 5 for each vertex v_p in \mathcal{V}^t is leveraged for the iteration step of the task-specific CDS extraction. Specifically, by leveraging the pre-computation of \mathbf{R}_p^m and the rotation estimations in \mathcal{V}^s connected by \mathcal{E}_p , the relative rotations on \mathcal{E}_p could be recomputed and compared with the corresponding measurements for edge supporting set \mathcal{E}_p^m acquisition:

$$\mathcal{E}_p^m = \{d_{\mathbf{R}}(\mathbf{R}_{n,p}, \mathbf{R}_p^m \mathbf{R}_n^\top) < \theta_{\text{th}} | v_n \in \mathcal{V}^s, e_{n,p} \in \mathcal{E}_p\}. \quad (6)$$

Then, the selection reward for edge $e_{m,p}$ is computed by:

$$\text{rwd}(m, p) = \sum_{\substack{v_n \in \mathcal{V}^s \\ e_{n,p} \in \mathcal{E}_p^m}} \cos(d_{\mathbf{R}}(\mathbf{R}_{n,p}, \mathbf{R}_p^m \mathbf{R}_n^\top)), \quad (7)$$

and the edges(vertices) $e_{m^*,p}(v_{m^*})$ and $e_{m^*,p^*}(v_{p^*})$ for the vertex v_p 's rotation pre-computation and the iteration step's NBV determination are selected by:

$$\begin{cases} v_{m^*} = \arg \max_{v_m \in \mathcal{V}^s} \text{rwd}(m, p), \\ v_{p^*} = \arg \max_{v_p \in \mathcal{V}^t} \text{rwd}(m^*, p). \end{cases} \quad (8)$$

Then, the absolute rotation of the selected NBV v_{p^*} could be initialized by $\mathbf{R}_{m^*,p^*} \mathbf{R}_{m^*}$. After NBV selection and initialization, optimization is further performed for accuracy and robustness improvement of the task-specific CDS construction. During the optimization procedure, local optimization on each newly selected NBV v_{p^*} is continuously performed and global optimization on all the currently estimated vertices $\{v_{p^*}\} \cup \mathcal{V}^s$ is intermittently carried out once the size of $|\{v_{p^*}\} \cup \mathcal{V}^s|$ having grown by a certain rate, say 5%. Specifically, for the local optimization, the inlier edge set for providing optimization constraints is first obtained by:

$$\mathcal{E}_{p^*}^m = \left\{ d_{\mathbf{R}}(\mathbf{R}_{n,p^*}, \mathbf{R}_{p^*}^m \mathbf{R}_n^\top) < \theta_{\text{th}} \mid v_n \in \mathcal{V}^s, e_{n,p^*} \in \mathcal{E}_{p^*} \right\}, \quad (9)$$

where $\mathbf{R}_{p^*}^m = \mathbf{R}_{m^*,p^*} \mathbf{R}_{m^*}$ is the rotation initialization of the vertex v_{p^*} . Then, the absolute rotation of v_{p^*} is locally optimized by:

$$\mathbf{R}_{p^*}^* = \arg \min \sum_{\substack{v_n \in \mathcal{V}^s \\ e_{n,p^*} \in \mathcal{E}_{p^*}^m}} d_{\mathbf{R}}^2(\mathbf{R}_{n,p^*}, \mathbf{R}_{p^*} \mathbf{R}_n^\top). \quad (10)$$

For the global optimization, the inlier edge set is also obtained:

$$(\mathcal{E}_{p^*} \cup \mathcal{E}^s)^* = \left\{ d_{\mathbf{R}}(\mathbf{R}_{m,n}, \mathbf{R}_n \mathbf{R}_m^\top) < \theta_{\text{th}} \right\} \quad (11)$$

for $v_m, v_n \in \{v_{p^*}\} \cup \mathcal{V}^s, e_{m,n} \in \mathcal{E}_{p^*} \cup \mathcal{E}^s$,

where \mathcal{E}^s is the edge set of \mathcal{V}^s . Then, the absolute rotations of the vertices in $\{v_{p^*}\} \cup \mathcal{V}^s$ are globally optimized by:

$$\{\mathbf{R}_m^*\} = \arg \min \sum_{\substack{v_m, v_n \in \{v_{p^*}\} \cup \mathcal{V}^s \\ e_{m,n} \in (\mathcal{E}_{p^*} \cup \mathcal{E}^s)^*}} d_{\mathbf{R}}^2(\mathbf{R}_{m,n}, \mathbf{R}_n \mathbf{R}_m^\top). \quad (12)$$

B. Other Key Steps Stemming from the IRAv3+

As the main difference between IRAv3+ [24] and IRAv4 proposed in this paper is the manner of global reference construction, the other key steps of IRAv4 stemming from IRAv3+ are described in this sub-section for better understanding.

Community detection-based cluster seed construction: With the objective of performing the following on-the-fly EG clustering and local rotation averaging, several cluster seeds should be constructed in advance for the cluster growing procedure. In both IRAv3 [23] and IRAv3+, they are constructed based on the community detection method [36]. Specifically, the above community detection method is performed on the input EG to generate community-based structure, and for each sub-EG of the community, camera triplet is selected, together with their absolute rotations estimated, which is similar to the initialization step of the task-specific CDS-based global reference construction in IRAv4 (cf. Eq. 1 to Eq. 4).

On-the-fly EG clustering and local rotation averaging: This step is first adopted in IRAv3, which is similar in principle to the iteration step of the task-specific CDS-based

⁴<http://www.ceres-solver.org/>

global reference construction in IRAv4 (*cf.* Eq. 5 to Eq. 12). To achieve this, for each unaffiliated vertex, the edge set between it and the currently affiliated vertex set of each cluster is first obtained. Then, by leveraging these edge sets, the supporting edge set of each unaffiliated vertex within each cluster could be obtained by absolute rotation pre-computation (*cf.* Eq. 5) and relative rotation re-computation (*cf.* Eq. 6). On this basis, the next-best affiliated vertex, together with its affiliated cluster and initialized rotation are simultaneously determined by supporting set global maximization (*cf.* Eq. 7 and Eq. 8). Then, the rotation estimation are locally (only on the next-best affiliated vertex) or globally (on all the vertices of the affiliated cluster) optimized (*cf.* Eq. 9 to Eq. 12). The above procedure is iteratively performed until all the vertices are affiliated, together with their rotations estimated.

Common vertices-guided alignment rotation estimation: After reference construction and EG clustering, cluster-to-reference rotation is estimated for local absolute rotation alignment. As observed in IRAv3+ that the rotation averaging-based absolute rotation estimates are more accurate and reliable than those of the essential matrix decomposition-based relative ones, a common vertices-guided alignment rotation estimation method is proposed. For a particular cluster, either one common vertex or one shared edge between it and the reference could induce an estimate of the cluster-to-reference alignment rotation. As the common vertices-induced ones are with higher priority, they are served as guidance for alignment rotation estimation. Specifically, for each vertex-induced estimate, one could obtain its supporters from the edge-induced ones, and the one with most supporters is used as the initialization of the alignment rotation, which is further optimized by leveraging the constraints provided by its supporters. Readers may refer to the original paper of IRAv3+ [23] for more details.

Local absolute rotation global alignment and optimization: Given the alignment rotation of each cluster, the absolute rotations in the cluster's local coordinate system are globally aligned to the reference's coordinate system. After that, inlier edge set of the original EG is firstly obtained based on the aligned rotations and then used for providing constraints for globally optimizing them (*cf.* Eq. 11 and Eq. 12).

IV. NEW ROTATION AVERAGING BENCHMARK CREATION

It could be observed that most of the existing rotation averaging methods [26], [27], [28], [29], [16], [21], [30], [19], [31], [22], [23], [24] perform performance evaluation based on the 1DSfM [32] dataset with the slightly outdated Bundler's [33] camera calibration results serving as the ground-truth source of camera rotations, which has been presented for more than ten years. In order to give a more comprehensive evaluation on the existing mainstream rotation averaging methods, a new 1DSfM-derived benchmark based on COLMAP [6] is rebuilt here. COLMAP is a general-purpose, end-to-end image-based 3D reconstruction pipeline with a graphical and command-line interface, which is proposed more recently and updated more frequently. In recent years, COLMAP has become the most widely recognized and commonly used open-source SfM toolbox with various downstream applications, such as novel view

synthesis [38], [39] and neural surface reconstruction [40], [41]. As a result, we believe that it is time for COLMAP to take the place of Bundler for rotation averaging benchmarking. The new benchmark creation process mainly contains three parts: epipolar-geometry graph regeneration, ground-truth data acquisition, and evaluation metrics definition, which are thoroughly described in the following, respectively.

A. Epipolar-Geometry Graph Regeneration

In order to present a new rotation averaging benchmark by making full use of COLMAP, the Epipolar-geometry Graph (EG) of each test data in the 1DSfM dataset is regenerated at first. It should be noted that only the images in the Maximum Connected Component (MCC) are considered during the EG regeneration procedure here for the efficiency consideration, and this image connectivity information is provided by the cc.txt file contained in the original 1DSfM dataset. Then, the images to be processed are fed into the COLMAP toolbox for local feature extraction and matching with default parameters. Given the pair-wise feature matches produced by COLMAP, OpenCV library is employed for essential matrix estimation and decomposition to produce relative motion (rotation and translation), where the feature-level point to epipolar line distance threshold and the desirable level of estimation confidence are set to 1pixel and 99.9% respectively during the RANdom SAmple Consensus (RANSAC) [42] procedure of the essential matrix estimation [10] process. After that, the image pair with more than 16 pairs of inlier feature matches for RANSAC-based essential matrix estimation is added as a graph edge to the regenerated EG. It should be further noted that the camera intrinsic parameters are required during essential matrix estimation, which are provided by the coords.txt file contained in the original 1DSfM dataset here.

B. Ground-Truth Data Acquisition

After EG regeneration, COLMAP is employed again for the ground-truth data acquisition of camera absolute rotations (and locations) for rotation averaging evaluation. Specifically, for each test data of the 1DSfM dataset, given the image matching result of COLMAP itself obtained in the last subsection, the SfM procedure integrated in COLMAP is conducted with default parameters, and the camera calibration result is denoted as $\{\mathbf{R}_i^C, \mathbf{c}_i^C | v_i \in \mathcal{V}_C\}$, where \mathcal{V}_C is the set of cameras successfully registered by COLMAP. In addition, the camera calibration result of Bundler, provided by the gt_bundle.out file contained in the original 1DSfM dataset, is denoted as $\{\mathbf{R}_j^B, \mathbf{c}_j^B | v_j \in \mathcal{V}_B\}$. It should be noted that $\{\mathbf{R}_j^B, \mathbf{c}_j^B\}$ has been aligned to the GPS coordinate system and is with real physical scale, while $\{\mathbf{R}_i^C, \mathbf{c}_i^C\}$ suffers from the issue of scale ambiguity due to the metric reconstruction nature of SfM. As a result, in order to use the camera calibration result of COLMAP as ground-truth camera poses for rotation (and translation) averaging evaluation, it should be aligned to the coordinate system of Bundler for scale recovery. The alignment is achieved by estimating a similarity transformation $\mathbf{T}_{C,B} = \begin{pmatrix} \mathbf{s}_{C,B} \mathbf{R}_{C,B} & \mathbf{t}_{C,B} \\ \mathbf{0}^\top & 1 \end{pmatrix}$ [43] based on RANSAC with the co-calibrated cameras by COLMAP and Bundler, $\mathcal{V}_{C \cap B}$, where

TABLE I

METADATA OF THE NEW 1DSFM-DERIVED ROTATION AVERAGING BENCHMARK, WHERE $|\mathcal{V}|$ AND $|\mathcal{V}_{\text{MCC}}|$ DENOTE THE NUMBER OF IMAGES IN THE ORIGINAL 1DSFM DATASET AND THAT IN THE MAXIMUM CONNECTED COMPONENT (MCC), $|\mathcal{V}_C|$, $|\mathcal{V}_B|$, AND $|\mathcal{V}_{C \cap B}|$ DENOTE NUMBER OF IMAGES REGISTERED BY COLMAP, BUNDLER, AND BOTH OF THEM, $e_R^{C \cap B}$ AND $e_c^{C \cap B}$ DENOTE THE COLMAP-TO-BUNDLER ALIGNMENT MEDIAN ERRORS OF ROTATION AND LOCATION IN DEGREE AND METER FOR THEIR CO-CALIBRATED CAMERAS, $|\mathcal{V}_{C \cap B}^h|$, $|\mathcal{V}_{C \cap B}^m|$, AND $|\mathcal{V}_{C \cap B}^c|$ DENOTE THE NUMBER OF IMAGES THAT PASS THE CROSS CHECK WITH HIGH, MEDIAN, AND COARSE LEVEL OF ACCURACY, AND $|\mathcal{E}|$, $e_R^{\mathcal{E}}$, AND $e_t^{\mathcal{E}}$ DENOTE THE NUMBER OF EDGES IN THE REGENERATED EPIPOLAR-GEOMETRY GRAPH (EG) AND THE MEDIAN ERRORS OF THE RELATIVE ROTATION AND TRANSLATION IN DEGREES.

Data	$ \mathcal{V} $	$ \mathcal{V}_{\text{MCC}} $	$ \mathcal{V}_C $	$ \mathcal{V}_B $	$ \mathcal{V}_{C \cap B} $	$e_R^{C \cap B}$	$e_c^{C \cap B}$	$ \mathcal{V}_{C \cap B}^h $	$ \mathcal{V}_{C \cap B}^m $	$ \mathcal{V}_{C \cap B}^c $	$ \mathcal{E} $	$e_R^{\mathcal{E}}$	$e_t^{\mathcal{E}}$
ALM	2915	627	585	577	563	0.64°	0.32m	244	332	522	72544	5.03°	8.53°
ELS	2587	247	239	227	226	0.29°	0.48m	61	116	212	15106	2.47°	8.79°
GDM	1463	742	709	677	670	1.19°	2.50m	51	125	395	31504	3.86°	7.65°
MDR	1344	394	333	341	321	0.82°	1.39m	24	64	255	15658	7.08°	13.38°
MND	2298	474	464	450	446	0.41°	0.21m	263	340	430	37063	2.34°	5.32°
NYC	2550	376	352	332	327	0.38°	0.22m	185	232	308	15104	3.72°	7.13°
PDP	2251	354	349	338	335	0.52°	0.37m	115	203	322	21434	2.10°	4.17°
PIC	7351	2508	2292	2152	2092	0.30°	0.26m	1020	1412	2013	267246	4.68°	10.23°
ROF	2364	1134	1103	1084	1063	0.18°	0.21m	592	758	994	61713	4.41°	7.89°
TOL	1576	508	469	472	449	0.29°	0.49m	92	228	380	22716	3.63°	4.48°
TFG	15685	5433	5061	5058	4869	0.24°	1.24m	162	742	4197	1056735	4.19°	9.52°
USQ	5961	930	869	789	769	1.03°	1.24m	139	266	599	33942	4.23°	23.52°
VNC	6288	918	862	836	808	0.90°	0.63m	164	337	725	72884	3.58°	8.35°
YKM	3368	458	432	437	422	0.65°	0.48m	71	225	373	18417	3.74°	7.20°

the locational distance threshold and the desirable estimation confidence are set to 1m and 99.9%, respectively. Then, based on the estimated transformation $\mathbf{T}_{C,B}$, $\{\mathbf{R}_i^C, \mathbf{c}_i^C\}$ could be aligned to $\{\mathbf{R}_j^B, \mathbf{c}_j^B\}$ by:

$$\left\{ \mathbf{R}_i^{C^*} = \mathbf{R}_i^C \mathbf{R}_{C,B}^\top, \mathbf{c}_i^{C^*} = s_{C,B} \mathbf{R}_{C,B} \mathbf{c}_i^C + \mathbf{t}_{C,B} \mid v_i \in \mathcal{V}_C \right\}. \quad (13)$$

Before performing rotation averaging method benchmarking, it should be further noticed that the basic assumption of involving the camera calibration result of the incremental SfM methods (Bundler or COLMAP) to serve as ground-truth source for motion (rotation and translation) averaging evaluation lies in that the camera orientation and localization results of incremental SfM with iterative RANSAC-based outlier filtering and BA-based parameter optimization [44] are acknowledged to be with much higher accuracy than those of motion averaging before performing the final global BA. Nonetheless, the incremental SfM-based calibration result inevitably contains estimation errors and is still not the real ground-truth camera poses. To make the evaluation with more reliability, inspired by the work of long-term visual localization benchmarking [45], the camera poses calibrated by COLMAP that pass Bundler-based cross check with certain pose accuracy level are used as the final camera pose ground-truth data. Its basic idea lies in that the camera poses calibrated by both COLMAP and Bundler with enough closeness in the 6-dimensional camera pose space are used for the following rotation averaging evaluation. Specifically, given the rotational ($\theta_{\text{th}}^{\text{h|m|c}}$) and locational ($d_{\text{th}}^{\text{h|m|c}}$) distance thresholds with different accuracy levels of camera poses: high-accuracy (2°, 0.25m), medium-accuracy (5°, 0.5m), and coarse-accuracy (10°, 5m), the camera subsets for rotation averaging evaluation with respect to the different distance thresholds are obtained by:

$$\mathcal{V}_{C \cap B}^{\text{h|m|c}} = \left\{ d_{\mathbf{R}}(\mathbf{R}_k^{C^*}, \mathbf{R}_k^B) < \theta_{\text{th}}^{\text{h|m|c}} \cap d_{\mathbf{c}}(\mathbf{c}_k^{C^*}, \mathbf{c}_k^B) < d_{\text{th}}^{\text{h|m|c}} \right\} \text{ for } v_k \in \mathcal{V}_{C \cap B}, \text{ where } d_{\mathbf{c}}(\mathbf{c}_1, \mathbf{c}_2) = \|\mathbf{c}_1 - \mathbf{c}_2\|_2. \quad (14)$$

The sizes of the camera subsets $\mathcal{V}_{C \cap B}^{\text{h|m|c}}$ together with some other meta-data about the new rotation averaging benchmark are listed in Table I, and in order to make a trade-off between ground-truth data magnitude and reliability, the camera subset with medium-accuracy, *i.e.* $\mathcal{V}_{C \cap B}^m$, are finally employed for rotation averaging benchmarking. The COLMAP-to-Bundler alignment median errors of rotation and location in Table I are defined as:

$$\begin{cases} e_R^{C \cap B} = \text{med}(\{d_{\mathbf{R}}(\mathbf{R}_k^{C^*}, \mathbf{R}_k^B) \mid v_k \in \mathcal{V}_{C \cap B}\}), \\ e_c^{C \cap B} = \text{med}(\{d_{\mathbf{c}}(\mathbf{c}_k^{C^*}, \mathbf{c}_k^B) \mid v_k \in \mathcal{V}_{C \cap B}\}), \end{cases} \quad (15)$$

where $\text{med}(\{x_i\})$ returns the median value of the set $\{x_i\}$. It could be further observed from the table that: 1) in most cases, except for MDR, TOL, and YKM, more cameras could be registered by COLMAP than Bundler; 2) the disparity in camera calibration accuracy between COLMAP and Bundler is insignificant as both $e_R^{C \cap B}$ and $e_c^{C \cap B}$ are relatively small; 3) Different test data in the new benchmark is with different degree of conformity in accuracy ($\frac{|\mathcal{V}_{C \cap B}^{\text{h|m|c}}|}{|\mathcal{V}_{C \cap B}|}$) between COLMAP and Bundler, take $\frac{|\mathcal{V}_{C \cap B}^m|}{|\mathcal{V}_{C \cap B}|}$ for example, 76.23% co-calibrated cameras pass the median-level-accuracy cross check for MND, while for TFG, that value decreases to only 15.24%.

C. Evaluation Metrics Definition

For a particular rotation averaging method X (what X could be is described in the next section), it is firstly performed on the relative rotations from the regenerated EG in this paper to obtain the absolute camera rotations. Then, based on the rotation averaging result and the relative translation measurements, translation averaging is performed with the mainstream method, BATA⁵ [34], to get the absolute camera locations, and the X-based motion averaging result is denoted as $\{\mathbf{R}_i^X, \mathbf{c}_i^X \mid v_i \in \mathcal{V}_X\}$. Then, the rotation \mathbf{R}_{X,C^*} and similarity transformation \mathbf{T}_{X,C^*} for aligning $\{\mathbf{R}_i^X, \mathbf{c}_i^X\}$ to the coordinate system of $\{\mathbf{R}_i^C, \mathbf{c}_i^C\}$ are estimated by the

⁵<https://bbzh.github.io/>

TABLE II

COMPARATIVE EXPERIMENT RESULTS IN ABSOLUTE ROTATION ESTIMATION ACCURACY AMONG SEVERAL MAIN-STREAM ROTATION AVERAGING METHODS ON THE NEW 1DSFM-DERIVED ROTATION AVERAGING BENCHMARK PROPOSED IN THIS PAPER: FIRST SECOND THIRD FORTH .

Data	IRLS-GM [35]	IRLS- $\ell_{\frac{1}{2}}$ [26]	MPLS [27]	DESC [31]	HARA [30]	NeuRoRA [28]	IRA [21]	IRA++ [22]	IRAv3 [23]	IRAv3+ [24]	IRAv4	MPLS w/ BA	IRAv4 w/ BA
ALM	1.22°	1.28°	1.20°	1.24°	1.33°	2.68°	1.33°	1.31°	1.32°	1.52°	1.23°	0.30°	0.22°
ELS	0.43°	0.36°	0.37°	0.48°	0.38°	0.95°	0.36°	0.37°	0.37°	0.37°	0.34°	0.11°	0.10°
GDM	1.72°	1.97°	1.10°	1.11°	2.69°	7.27°	1.36°	0.90°	0.77°	2.58°	0.75°	0.29°	0.28°
MDR	0.75°	0.92°	0.75°	0.78°	0.78°	4.20°	0.86°	1.77°	1.05°	1.50°	0.68°	0.22°	0.32°
MND	0.57°	0.50°	0.54°	0.53°	0.48°	1.11°	0.53°	0.56°	0.54°	0.54°	0.51°	0.11°	0.11°
NYC	0.98°	1.06°	0.99°	1.05°	1.00°	1.87°	1.25°	1.47°	1.29°	1.37°	1.18°	0.17°	0.12°
PDP	0.58°	0.53°	0.54°	0.53°	0.52°	1.06°	0.58°	0.67°	0.53°	0.51°	0.53°	0.10°	0.10°
PIC	1.39°	1.72°	1.38°	1.41°	1.66°	37.98°	1.49°	1.48°	1.37°	2.47°	1.46°	0.54°	0.86°
ROF	1.58°	1.58°	1.56°	1.54°	1.53°	14.43°	6.36°	6.70°	4.39°	5.79°	2.42°	0.48°	1.21°
TOL	2.66°	1.98°	3.08°	3.55°	3.31°	3.61°	2.26°	2.99°	2.44°	2.33°	2.73°	1.93°	1.54°
TFG	1.46°	1.57°	1.51°	1.45°	1.78°	24.25°	1.12°	1.75°	1.07°	1.42°	1.10°	1.01°	0.76°
USQ	6.67°	1.70°	6.99°	7.04°	1.60°	16.76°	4.44°	4.89°	4.19°	3.95°	3.95°	3.25°	3.69°
VNC	0.71°	0.66°	0.71°	0.71°	0.69°	1.72°	0.99°	1.08°	1.02°	1.14°	0.94°	0.10°	0.27°
YKM	1.96°	2.05°	1.87°	1.94°	1.85°	5.65°	1.99°	3.30°	1.67°	2.78°	1.81°	0.22°	0.42°
Rank	5.29	4.64	4.43	5.21	5.00	11.00	5.86	7.86	4.64	6.79	3.43	1.43	1.43

TABLE III

COMPARATIVE RESULTS IN ROTATION ESTIMATION ACCURACY ON THE ORIGINAL 1DSFM DATASET: FIRST SECOND THIRD FORTH .

Data	RAGO [19]	IRA [21]	IRA++ [22]	IRAv3 [23]	IRAv3+ [24]	IRAv4
ALM	0.83°	0.88°	0.80°	0.73°	0.72°	0.74°
ELS	0.46°	0.51°	0.46°	0.44°	0.39°	0.41°
GDM	2.68°	5.32°	2.88°	1.99°	2.20°	2.12°
MDR	1.03°	0.85°	0.83°	0.75°	0.75°	0.74°
MND	0.46°	0.51°	0.50°	0.44°	0.40°	0.40°
NYC	0.71°	1.00°	0.95°	0.82°	0.81°	0.77°
PDP	0.63°	0.90°	0.75°	0.72°	0.63°	0.62°
PIC	0.58°	1.67°	1.70°	1.50°	1.55°	1.42°
ROF	1.10°	1.51°	1.24°	1.09°	1.14°	0.96°
TOL	1.20°	2.45°	1.33°	1.44°	1.09°	1.11°
TFG	1.53°	3.30°	1.74°	1.49°	1.80°	1.79°
USQ	1.92°	4.40°	3.70°	3.27°	2.77°	3.15°
VNC	0.89°	1.02°	0.94°	0.86°	0.76°	0.81°
YKM	0.92°	1.57°	1.38°	1.36°	0.98°	1.20°
Rank	3.00	5.79	4.64	2.93	2.29	2.07

methods of voting-based single rotation averaging [29] and RANSAC-based similarity estimation, respectively. The pose alignment is conducted in the same way of Eq. 13, and the aligned poses are denoted as $\{\mathbf{R}_i^{\text{X}^*}, \mathbf{c}_i^{\text{X}^*}\}$. Finally, the median rotational and locational errors on the camera subset of $\mathcal{V}_{\text{C}\cap\text{B}}^{\text{m}}$ are served as the evaluation metrics of the new rotation averaging benchmark, which are defined as:

$$\begin{cases} e_{\mathbf{R}}^{\text{X}} = \text{med}(\{d_{\mathbf{R}}(\mathbf{R}_k^{\text{X}^*}, \mathbf{R}_k^{\text{C}^*})|v_k \in \mathcal{V}_{\text{C}\cap\text{B}}^{\text{m}}\}), \\ e_{\mathbf{c}}^{\text{X}} = \text{med}(\{d_{\mathbf{c}}(\mathbf{c}_k^{\text{X}^*}, \mathbf{c}_k^{\text{C}^*})|v_k \in \mathcal{V}_{\text{C}\cap\text{B}}^{\text{m}}\}). \end{cases} \quad (16)$$

V. ROTATION AVERAGING METHOD BENCHMARKING

In this section, several mainstream rotation averaging methods for comparison are first introduced, and then rotation averaging method benchmarking in terms of rotation and location estimation is performed based on the presented new rotation averaging benchmark.

A. Rotation Averaging Methods for Comparison

Except for the IRA series (IRA [21], IRA++ [22], IRAv3 [23], IRAv3+ [24], and IRAv4 proposed in this paper)

which have been described in Sec. II and Sec. III, there are some other mainstream rotation averaging methods involved in this section for comparison, including IRLS-GM⁶ [35], IRLS- $\ell_{\frac{1}{2}}$ ⁶ [26], MPLS⁷ [27], DESC⁸ [31], HARA⁹ [30], and NeuRoRA¹⁰ [28]. These methods are briefly introduced in the following for better understanding.

IRLS-GM [35] works on the Lie group structure of rotations and solves the problem of large-scale robust rotation averaging in a two-stage manner. ℓ_1 -based optimization is first carried out to achieve an efficient, scalable, and robust solution. Based-on the ℓ_1 -based initialization, Iterative Reweighted Least Squares (IRLS)-based optimization with the Geman-McClure (GM) loss function is performed to further improve the accuracy of the solution.

IRLS- $\ell_{\frac{1}{2}}$ [26] is the upgrade version of IRLS-GM, which also contains two steps. IRLS-GM and IRLS- $\ell_{\frac{1}{2}}$ share the same step one. For the second step of IRLS- $\ell_{\frac{1}{2}}$, a fairly exhaustive evaluation of the performance of a variety of robust loss functions that are popular in the statistical literature is provided, which leads to a recommendation of the $\ell_{\frac{1}{2}}$ loss function that provides the best empirical performance.

MPLS [27] is a framework that could be served as alternative paradigm to IRLS for rotation averaging under high corruption and noise. It uses the theoretically guaranteed cycle-edge message passing algorithm for estimating the underlying corruption levels. These estimates are then used for learning better weights for the weighted least squares problem. The limitations of IRLS and the advantages of MPLS for solving the rotation averaging are also discussed and analyzed in the original paper of MPLS.

DESC [31] is a novel quadratic programming formulation for estimating the corruption levels in rotation averaging, which are used for solving this problem. Its objective function exploits the cycle consistency of the Lie group and has the

⁶<https://ee.iisc.ac.in/cvlab/research/rotaveraging/>

⁷<https://github.com/yunpeng-shi/MPLS>

⁸<https://github.com/ColeWyeth/DESC>

⁹<https://github.com/sunghoon031/HARA>

¹⁰<https://github.com/pulak09/NeuRoRA>

TABLE IV

COMPARATIVE EXPERIMENT RESULTS IN ABSOLUTE LOCATION ESTIMATION ACCURACY AMONG SEVERAL MAIN-STREAM ROTATION AVERAGING METHODS ON THE NEW 1DSfM-DERIVED ROTATION AVERAGING BENCHMARK PROPOSED IN THIS PAPER: **FIRST** | **SECOND** | **THIRD** | **FOURTH**.

Data	IRLS-GM [35]	IRLS- ℓ_1 [26]	MPLS [27]	DESC [31]	HARA [30]	NeuRoRA [28]	IRA [21]	IRA++ [22]	IRAv3 [23]	IRAv3+ [24]	IRAv4	MPLS w/ BA	IRAv4 w/ BA
ALM	0.70m	0.70m	0.70m	0.71m	0.69m	0.72m	0.72m	0.71m	0.73m	0.72m	0.71m	0.32m	0.32m
ELS	3.52m	3.49m	3.54m	3.58m	3.48m	3.47m	3.36m	3.30m	3.30m	3.34m	3.36m	1.77m	1.69m
GDM	3.21m	2.03m	1.79m	1.65m	2.66m	6.15m	1.66m	1.47m	1.59m	1.51m	1.41m	0.53m	0.49m
MDR	1.47m	1.38m	1.26m	1.39m	1.32m	1.51m	1.84m	1.71m	1.23m	2.08m	1.31m	0.57m	0.55m
MND	0.68m	0.70m	0.69m	0.69m	0.69m	0.71m	0.67m	0.68m	0.68m	0.68m	0.67m	0.45m	0.45m
NYC	0.67m	0.68m	0.67m	0.67m	0.67m	0.71m	0.65m	0.66m	0.65m	0.63m	0.65m	0.37m	0.33m
PDP	0.80m	0.80m	0.80m	0.79m	0.80m	0.83m	0.86m	0.87m	0.83m	0.81m	0.85m	0.46m	0.44m
PIC	1.09m	1.08m	1.08m	1.08m	1.08m	4.70m	1.08m	1.09m	1.06m	1.23m	1.09m	0.56m	0.64m
ROF	7.01m	6.94m	7.02m	7.12m	6.99m	15.18m	7.24m	8.13m	7.89m	7.04m	6.53m	3.33m	3.10m
TOL	3.16m	2.87m	3.14m	3.29m	3.24m	3.05m	2.74m	3.33m	3.52m	3.21m	3.19m	1.15m	1.90m
TFG	3.95m	3.90m	4.02m	3.94m	4.28m	11.42m	3.90m	4.08m	3.97m	4.29m	3.91m	3.05m	2.84m
USQ	2.32m	2.55m	2.42m	2.31m	2.76m	12.58m	2.52m	2.55m	2.39m	2.81m	2.45m	0.65m	1.43m
VNC	1.34m	1.39m	1.30m	1.35m	1.33m	1.44m	1.33m	1.34m	1.35m	1.37m	1.35m	0.32m	0.42m
YKM	1.00m	1.00m	0.99m	0.98m	0.99m	1.10m	1.01m	1.06m	1.01m	1.01m	1.01m	0.48m	0.45m
Rank	5.00	5.21	4.36	5.07	5.07	9.36	4.79	6.57	5.07	6.64	4.21	1.57	1.29

following advantages: 1) It can tolerate corruption as high as the information-theoretic bound; 2) It does not require a good initialization for the estimates of group elements; 3) It has a simple interpretation; And 4) under some mild conditions its global minimum exactly recovers the corruption levels.

HARA [30] presents a hierarchical initialization scheme that constructs a spanning tree of a rotation graph by propagating most reliable constraints first and less reliable ones later. In HARA, the hierarchy of reliability based on the number of consistent triplet constraints, as well as their level of consistency, is established. That is, a constraint is considered to be more reliable if it is strongly supported by many other constraints and less reliable if it has weaker or fewer supports. In addition, the number of valid 2D-2D correspondences could also be optionally incorporated into the hierarchy.

NeuRoRA [28] is built to learn patterns from the data and predict/regress the model parameters from the noisy relative rotation measurements. NeuRoRA is a two-step approach: In the first step, a graph-based network, CleanNet, is utilized to clean the EG by removing outliers and rectifying noisy measurements; And in the second step, an initialization from the cleaned EG, instantiated from a shortest path tree, is then further fine-tuned using a separate graph-based network, FineNet, to produce the final rotation averaging results.

B. Rotation Estimation Accuracy Benchmarking

For the methods of IRLS-GM, IRLS- ℓ_1 , MPLS, DESC, and HARA, we locally run the official source codes (with default parameters) released by the authors on the new 1DSfM-derived rotation averaging benchmark to produce the absolute rotation estimation results of them. For the method of NeuRoRA, follow the authors' instruction, the CleanNet and FineNet of NeuRoRA are both firstly pretrained on synthetic data and then finetuned and tested on the real-world data (with default parameters) in round-robin fashion (leave one out). And for the methods of existing IRA series (IRA, IRA++, IRAv3, and IRAv3+) and the proposed IRAv4, locally implemented source codes are employed for absolute rotation estimation. The absolute rotation estimation results of all the methods

for comparison on the new benchmark are shown in Table II. The top-four results on each test data among all the comparative methods are highlighted, and in order to perform a comprehensive comparison, the rankings of all the comparative methods on each test data are averaged and shown in the last row of the table, and the top-four methods are highlighted as well. It could be seen from the table that: 1) Among all the rotation averaging methods for comparison, the proposed IRAv4 in this paper achieves overall the best performance in rotation estimation accuracy on the new 1DSfM-derived rotation averaging benchmark; 2) The deep learning-based rotation averaging method NeuRoRA is rather data/domain-sensitive and performs relatively poor in rotation estimation accuracy on the new benchmark, especially for the large-scale (PIC, ROF, and TFG) and high-noise (GDM, MDR, and USQ) test data; And 3) Compared with the results of IRA++ and IRAv3+, better performance is achieved by IRAv3 and IRAv4 in rotation estimation accuracy on the new benchmark, which demonstrates the effectiveness of the *task-specific* epipolar-geometry graph clustering and alignment reference construction proposed in IRAv3 and IRAv4, respectively.

In addition, in order to further demonstrate the effectiveness of the proposed IRAv4, comparative experiments in rotation estimation accuracy on the original 1DSfM dataset are also conducted, and the results are shown in Table III. It could be observed that compared with the state-of-the-art method on the dataset, RAGO [19], and the existing IRA series, IRAv4 is able to achieve overall the best performance as well. And the reasons for the inconsistency of different methods in rotation estimation accuracy on the two benchmarks (*cf.* Table II and Table III) mainly lie in the differences in ground-truth rotation source (different number of cameras involved in evaluation and different ways in obtaining their ground-truth rotations).

C. Location Estimation Accuracy Benchmarking

Given the absolute rotation estimation results of all the rotation averaging methods for comparison on the new 1DSfM-derived benchmark (and the relative translations in the regenerated EG, which is mandatory for location estimation), we

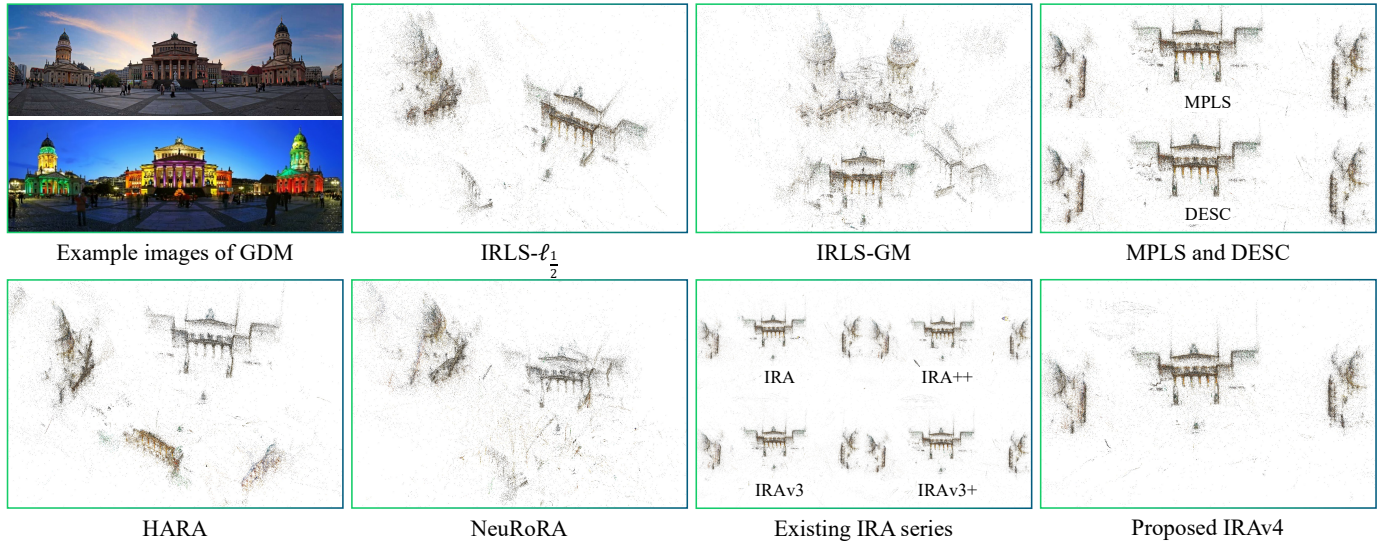


Fig. 2. Sparse scene reconstruction results of all rotation averaging methods for comparison on the test data of GDM of the new rotation averaging benchmark.

locally run the official source code of BATA (with default parameters) released by the authors to produce the absolute location estimation results of these methods. The absolute location estimation results of all the methods for comparison on the new benchmark are shown in Table IV. And similar to that in Table II, the top-four methods on each test data and in terms of overall rankings are highlighted. By observing the above two tables, similar conclusions, *i.e.* the three items discussed in the last sub-section, could be drawn. It could be further observed that though with moderately strong correlation, among different rotation averaging methods, the advantage in rotation estimation accuracy would not be strictly maintained during location estimation, *e.g.* the third and fourth-best methods in rotation estimation accuracy on the new benchmark are IRAv3 and IRLS- $\ell_{\frac{1}{2}}$, while those in location estimation accuracy are IRA and IRLS-GM.

D. Incorporation of the Global Bundle Adjustment

In order to demonstrate the performance of different rotation averaging methods coupled with some certain translation averaging method (BATA) in providing accurate enough camera pose initializations for the final BA, multi-view triangulation-based scene computation and global BA-based pose optimization are performed. Specifically, the pair-wise feature matches those pass through the RANSAC-based essential matrix estimation are linked to feature tracks with the union find algorithm implemented in OpenMVG¹¹. Then, a RANSAC-based multi-view triangulation algorithm implemented in COLMAP is performed with the reprojection error and viewing angle thresholds, and the desirable level of estimation confidence setting to 4pixel, 2°, and 99.9% to compute the initial values of the feature tracks' spatial coordinates. During the multi-view triangulation, the intrinsic parameters provided by the original 1DSfM dataset, and the camera poses estimated by different rotation averaging methods and BATA are used to

formulate camera projection matrices. Finally, given the initial values of camera parameters and scene points, global BA is performed to further improve the camera pose accuracy, which is conducted by leveraging Ceres Solver with Huber loss. The rotation and location estimation accuracy of the optimized camera poses of the top-2 methods in both rotation and location estimation accuracy before global BA (IRAv4 and MPLS) on the new benchmark are shown in the last two columns of Table II and Table IV, respectively. Note that the results of them are re-ranked independently in the tables to maintain comparative fairness. It could be observed from the two tables that with the global BA, the camera pose estimation accuracy of both IRAv4 and MPLS is largely improved, and IRAv4 achieves slightly better performance in location estimation accuracy than MPLS, which demonstrates that accurate enough camera pose initializations could be provided by both IRAv4 and MPLS coupling BATA, and the advantage of IRAv4 over MPLS.

Furthermore, to provide a more intuitive comparison in robustness of all the rotation averaging methods for comparison, the sparse scene reconstruction results after global BA of them on the test data of GDM of the new rotation averaging benchmark are shown in Fig. 2. As shown in the upper-left of this figure, there are two buildings with left-right symmetry located in the scene of GDM, which significantly increases the difficulty of camera pose estimation and the subsequent scene structure recovery. It could be observed from the figure that among all 11 rotation averaging methods involved in benchmarking, only MPLS, DESC, and the IRA series succeed to recover the correct scene structure of GDM, which demonstrate their robustness.

VI. CONCLUSION

In this paper, to benefit from the global reference for local-to-global rotation alignment more, an incremental parameter estimation-based task-specific connected dominating set extraction method is proposed, by which the accuracy and

¹¹<https://github.com/openMVG/openMVG>

robustness of the Incremental Rotation Averaging (IRA) series are further advanced. Furthermore, a new 1DSfM-derived rotation averaging benchmark, together with new ground-truth data acquisition approach, and new evaluation tasks and metrics, based on the camera calibration results of COLMAP is presented, in order to give a more comprehensive and reasonable comparison among different rotation averaging methods. Based on the new benchmark, the proposed method in this paper, IRAv4, achieves overall the best performance in both rotation and downstream location estimation, which demonstrates its effectiveness in terms of accuracy and robustness when dealing with large-scale and high-noise rotation averaging problems.

REFERENCES

- [1] X. Gao, S. Shen, Y. Zhou, H. Cui, L. Zhu, and Z. Hu, "Ancient Chinese architecture 3D preservation by merging ground and aerial point clouds," *ISPRS Journal of Photogrammetry and Remote Sensing*, vol. 143, pp. 72–84, 2018. [1](#)
- [2] X. Gao, S. Shen, L. Zhu, T. Shi, Z. Wang, and Z. Hu, "Complete scene reconstruction by merging images and laser scans," *IEEE Transactions on Circuits and Systems for Video Technology*, vol. 30, no. 10, pp. 3688–3701, 2020. [1](#)
- [3] X. Gao, L. Zhu, B. Fan, H. Liu, and S. Shen, "Incremental translation averaging," *IEEE Transactions on Circuits and Systems for Video Technology*, vol. 32, no. 11, pp. 7783–7795, 2022. [1](#)
- [4] X. Gao, D. Tao, Y. Liu, Z. Xie, and S. Shen, "Vehicle-borne multi-sensor temporal–spatial pose globalization via cross-domain data association," *IEEE Transactions on Intelligent Transportation Systems*, pp. 1–14, 2023. [1](#)
- [5] Z. Cui and P. Tan, "Global structure-from-motion by similarity averaging," in *IEEE International Conference on Computer Vision (ICCV)*, 2015, pp. 864–872. [1](#)
- [6] J. L. Schönberger and J. M. Frahm, "Structure-from-motion revisited," in *IEEE Conference on Computer Vision and Pattern Recognition (CVPR)*, 2016, pp. 4104–4113. [1, 2, 5](#)
- [7] H. Cui, X. Gao, S. Shen, and Z. Hu, "HSfM: Hybrid structure-from-motion," in *IEEE Conference on Computer Vision and Pattern Recognition (CVPR)*, 2017, pp. 2393–2402. [1](#)
- [8] H. Cui, S. Shen, X. Gao, and Z. Hu, "Batched incremental structure-from-motion," in *International Conference on 3D Vision (3DV)*, 2017, pp. 205–214. [1](#)
- [9] S. Zhu, R. Zhang, L. Zhou, T. Shen, T. Fang, P. Tan, and L. Quan, "Very large-scale global SfM by distributed motion averaging," in *IEEE Conference on Computer Vision and Pattern Recognition (CVPR)*, 2018, pp. 4568–4577. [1](#)
- [10] D. Nister, "An efficient solution to the five-point relative pose problem," *IEEE Transactions on Pattern Analysis and Machine Intelligence*, vol. 26, no. 6, pp. 756–770, 2004. [1, 5](#)
- [11] R. Hartley, J. Trumpf, Y. Dai, and H. Li, "Rotation averaging," *International Journal of Computer Vision*, vol. 103, p. 267–305, 2013. [1](#)
- [12] K. Wilson and D. Bindel, "On the distribution of minima in intrinsic-metric rotation averaging," in *IEEE/CVF Conference on Computer Vision and Pattern Recognition (CVPR)*, 2020, pp. 6030–6038. [1](#)
- [13] F. Dellaert, D. M. Rosen, J. Wu, R. Mahony, and L. Carlone, "Shonan rotation averaging: Global optimality by surfing $SO(p)^n$," in *European Conference on Computer Vision (ECCV)*, 2020, pp. 292–308. [1](#)
- [14] A. Eriksson, C. Olsson, F. Kahl, and T. J. Chin, "Rotation averaging with the chordal distance: Global minimizers and strong duality," *IEEE Transactions on Pattern Analysis and Machine Intelligence*, vol. 43, no. 1, pp. 256–268, 2021. [1](#)
- [15] Y. Chen, J. Zhao, and L. Kneip, "Hybrid rotation averaging: A fast and robust rotation averaging approach," in *IEEE/CVF Conference on Computer Vision and Pattern Recognition (CVPR)*, 2021, pp. 10358–10367. [1](#)
- [16] L. Yang, H. Li, J. A. Rahim, Z. Cui, and P. Tan, "End-to-end rotation averaging with multi-source propagation," in *IEEE/CVF Conference on Computer Vision and Pattern Recognition (CVPR)*, 2021, pp. 11774–11783. [1, 2, 5](#)
- [17] A. Parra, S.-F. Chng, T.-J. Chin, A. Eriksson, and I. Reid, "Rotation coordinate descent for fast globally optimal rotation averaging," in *IEEE/CVF Conference on Computer Vision and Pattern Recognition (CVPR)*, 2021, pp. 4296–4305. [1](#)
- [18] G. Moreira, M. Marques, and J. P. Costeira, "Rotation averaging in a split second: A primal-dual method and a closed-form for cycle graphs," in *IEEE/CVF International Conference on Computer Vision (ICCV)*, 2021, pp. 5432–5440. [1](#)
- [19] H. Li, Z. Cui, S. Liu, and P. Tan, "RAGO: Recurrent graph optimizer for multiple rotation averaging," in *IEEE/CVF Conference on Computer Vision and Pattern Recognition (CVPR)*, 2022, pp. 15787–15796. [1, 2, 5, 7, 8](#)
- [20] G. Zhang, V. Larsson, and D. Barath, "Revisiting rotation averaging: Uncertainties and robust losses," in *IEEE/CVF Conference on Computer Vision and Pattern Recognition (CVPR)*, 2023, pp. 17215–17224. [1](#)
- [21] X. Gao, L. Zhu, Z. Xie, H. Liu, and S. Shen, "Incremental rotation averaging," *International Journal of Computer Vision*, vol. 129, pp. 1202–1216, 2021. [1, 2, 3, 5, 7, 8](#)
- [22] X. Gao, L. Zhu, H. Cui, Z. Xie, and S. Shen, "IRAv+: Distributed incremental rotation averaging," *IEEE Transactions on Circuits and Systems for Video Technology*, vol. 32, no. 7, pp. 4885–4892, 2022. [1, 2, 5, 7, 8](#)
- [23] X. Gao, H. Cui, M. Li, Z. Xie, and S. Shen, "IRAv3: Hierarchical incremental rotation averaging on the fly," *IEEE Transactions on Circuits and Systems for Video Technology*, vol. 33, no. 4, pp. 2001–2006, 2023. [1, 2, 4, 5, 7, 8](#)
- [24] X. Gao, H. Cui, W. Huang, M. Li, and S. Shen, "IRAv3+: Hierarchical incremental rotation averaging via multiple connected dominating sets," *IEEE Transactions on Circuits and Systems for Video Technology*, pp. 1–8, 2023. [1, 2, 3, 4, 5, 7, 8](#)
- [25] S. Jiang, Q. Li, W. Jiang, and W. Chen, "Parallel structure from motion for UAV images via weighted connected dominating set," *IEEE Transactions on Geoscience and Remote Sensing*, vol. 60, p. 5413013, 2022. [1, 3](#)
- [26] A. Chatterjee and V. M. Govindu, "Robust relative rotation averaging," *IEEE Transactions on Pattern Analysis and Machine Intelligence*, vol. 40, no. 4, pp. 958–972, 2018. [2, 5, 7, 8](#)
- [27] Y. Shi and G. Lerman, "Message passing least squares framework and its application to rotation synchronization," in *International Conference on Machine Learning (ICML)*, 2020, pp. 8796–8806. [2, 5, 7, 8](#)
- [28] P. Purkait, T. J. Chin, and I. Reid, "NeuRoRA: Neural robust rotation averaging," in *European Conference on Computer Vision (ECCV)*, 2020, pp. 137–154. [2, 5, 7, 8](#)
- [29] X. Gao, J. Luo, K. Li, and Z. Xie, "Hierarchical RANSAC-based rotation averaging," *IEEE Signal Processing Letters*, vol. 27, pp. 1874–1878, 2020. [2, 5, 7](#)
- [30] S. H. Lee and J. Civera, "HARA: A hierarchical approach for robust rotation averaging," in *IEEE/CVF Conference on Computer Vision and Pattern Recognition (CVPR)*, 2022, pp. 15777–15786. [2, 5, 7, 8](#)
- [31] Y. Shi, C. Wyeth, and G. Lerman, "Robust group synchronization via quadratic programming," in *International Conference on Machine Learning (ICML)*, 2022, pp. 20095–20105. [2, 5, 7, 8](#)
- [32] K. Wilson and N. Snavely, "Robust global translations with 1DSfM," in *European Conference on Computer Vision (ECCV)*, 2014, pp. 61–75. [2, 5](#)
- [33] N. Snavely, S. M. Seitz, and R. Szeliski, "Modeling the world from Internet photo collections," *International Journal of Computer Vision*, vol. 80, no. 2, pp. 189–210, 2008. [2, 5](#)
- [34] B. Zhuang, L. Cheong, and G. H. Lee, "Baseline desensitizing in translation averaging," in *IEEE/CVF Conference on Computer Vision and Pattern Recognition (CVPR)*, 2018, pp. 4539–4547. [2, 6](#)
- [35] A. Chatterjee and V. M. Govindu, "Efficient and robust large-scale rotation averaging," in *IEEE International Conference on Computer Vision (ICCV)*, 2013, pp. 521–528. [2, 7, 8](#)
- [36] L. Zhou, Z. Luo, M. Zhen, T. Shen, S. Li, Z. Huang, T. Fang, and L. Quan, "Stochastic bundle adjustment for efficient and scalable 3D reconstruction," in *European Conference on Computer Vision (ECCV)*, 2020, pp. 364–379. [2, 4](#)
- [37] S. Guha and S. Khuller, "Approximation algorithms for connected dominating sets," *Algorithmica*, vol. 20, p. 374–387, 1998. [3](#)
- [38] R. Martin-Brualla, N. Radwan, M. S. M. Sajjadi, J. T. Barron, A. Dosovitskiy, and D. Duckworth, "NeRF in the wild: Neural radiance fields for unconstrained photo collections," in *IEEE/CVF Conference on Computer Vision and Pattern Recognition (CVPR)*, 2021, pp. 7206–7215. [5](#)
- [39] K. Deng, A. Liu, J. Zhu, and D. Ramanan, "Depth-supervised NeRF: Fewer views and faster training for free," in *IEEE/CVF Conference on Computer Vision and Pattern Recognition (CVPR)*, 2022, pp. 12872–12881. [5](#)

- [40] Y. Liu, L. Wang, J. Yang, W. Chen, X. Meng, B. Yang, and L. Gao, “NeUDF: Leaning neural unsigned distance fields with volume rendering,” in *IEEE/CVF Conference on Computer Vision and Pattern Recognition (CVPR)*, 2023, pp. 237–247. [5](#)
- [41] Y. Wang, I. Skorokhodov, and P. Wonka, “PET-NeuS: Positional encoding tri-planes for neural surfaces,” in *IEEE/CVF Conference on Computer Vision and Pattern Recognition (CVPR)*, 2023, pp. 12598–12607. [5](#)
- [42] M. A. Fischler and R. C. Bolles, “Random sample consensus: A paradigm for model fitting with applications to image analysis and automated cartography,” *Communications of the ACM*, vol. 24, no. 6, pp. 381–395, 1981. [5](#)
- [43] S. Umeyama, “Least-squares estimation of transformation parameters between two point patterns,” *IEEE Transactions on Pattern Analysis and Machine Intelligence*, vol. 13, no. 4, pp. 376–380, 1991. [5](#)
- [44] S. Agarwal, N. Snavely, S. M. Seitz, and R. Szeliski, “Bundle adjustment in the large,” in *European Conference on Computer Vision (ECCV)*, 2010, pp. 29–42. [6](#)
- [45] C. Toft, W. Maddern, A. Torii, L. Hammarstrand, E. Stenborg, D. Safari, M. Okutomi, M. Pollefeys, J. Sivic, T. Pajdla, F. Kahl, and T. Sattler, “Long-term visual localization revisited,” *IEEE Transactions on Pattern Analysis and Machine Intelligence*, vol. 44, no. 4, pp. 2074–2088, 2022. [6](#)